Journal of Power Sources 545 (2022) 231901

Contents lists available at ScienceDirect

Journal of Power Sources

journal homepage: www.elsevier.com/locate/jpowsour

Heat generation and degradation mechanisms studied on $Na_3V_2(PO_4)_3$/C positive electrode material in full pouch / coin cell assembly

Ijaz Ul Mohsin [a,*], Luca Schneider [b], Marcel Häringer [b], Carlos Ziebert [a], Magnus Rohde [a], Werner Bauer [b], Helmut Ehrenberg [b], Hans Jürgen Seifert [a]

[a] Institute for Applied Materials – Applied Materials Physics (IAM-AWP), Karlsruhe Institute of Technology, Karlsruhe, Germany
[b] Institute for Applied Materials – Energy Storage Systems (IAM-ESS), Karlsruhe Institute of Technology, Karlsruhe, Germany

HIGHLIGHTS

- $Na_3V_2(PO_4)_3$/C vs HC in coin and pouch cell formats are studied.
- The heat generation is measured both on pristine and cycled-aged cells.
- Identification and contribution of various resistances from cathode and anode.
- Describe the relationship between generated heat and the degradation of materials.
- The cell balancing shows a pronounced effect on the amount of generated heat.

ARTICLE INFO

Keywords:
Heat generation
Post lithium technology
Impedance
Degradation
Isothermal calorimetry

ABSTRACT

$Na_3V_2(PO_4)_3$/C cathode and commercial hard carbon anode materials are coated with a roll-to-roll coater on an aluminum current collector. Sodium-ion pouch and coin cells are assembled. The degradation mechanism, cycle stability, morphology of cycle-aged material, and aging influence on the heat generation during cycling are thoroughly investigated. Electrochemical impedance spectroscopy permits resistance assignment to the specific electrodes by using the distribution of relaxation times. Comparison of pristine and cycle-aged cells allows separating the degradation contributions of the particular electrodes. The generated heat during charging and discharging is determined by means of an advanced highly sensitive MS80 3D Tian-Calvet calorimeter under isothermal conditions at 25 °C and the heat generation mechanisms are elucidated. It is observed that less heat is generated during charging than discharging process. Furthermore, the cell balancing reveals a pronounced effect (approximately 50% in charging and 20% in discharging) on the amount of generated heat, which is valuable feedback for the material developers and cell designers. These analyses represent a fingerprint for the underlying electrochemical processes at the electrodes and are very essential for state of health, aging prediction as well as the subsequent tackling of safety-related issues in sodium-ion batteries.

1. Introduction

Since the demand for lithium batteries grows, the supply of precursor materials is under pressure and consequently, the prices of battery materials have increased in recent months as reported by BloombergNEF [1]. Therefore, an alternative battery technology system requires, particularly in electrochemical energy storage on a large scale. The abundance of sodium, coupled with a similar kinetic (a bit slower) mechanism (intercalation/de-intercalation), makes sodium a promising substitute for stationary lithium-ion batteries [2–4]. Like other battery devices, cathodes determine the electrochemical characteristics, safety, and of course cost of SIBs [5,6]. A promising cathode material is $Na_3V_2(PO_4)_3$ (NVP), due to its high energy density, cycle stability, and rate capability [7]. NVP is typical sodium super ionic conductor (NASICON) type material and like all these materials their electronic conductivity is low. NVP has a total conductivity of 1×10^{-6} S cm^{-1} at 2.9 V, which decreases to 8×10^{-8} S cm^{-1} at 3.5 V [8]. To overcome these problems different strategies are developed, like shrinking down

* Corresponding author. Hermann-von-Helmholtz-Platz 1, 76344, Eggenstein-Leopoldshafen, Germany.
E-mail address: ijaz.mohsin@kit.edu (I.U. Mohsin).

https://doi.org/10.1016/j.jpowsour.2022.231901
Received 13 June 2022; Received in revised form 19 July 2022; Accepted 25 July 2022
Available online 8 August 2022

the particle size [9,10], but the most common is the creation of a conductive carbon matrix [11]. In our case, we used porous NVP/C composites with carbon coating to create an electronic conductive network. Studies on heat generation of these and related electrode materials are required as suitable safety behavior is a prerequisite for the usage of the battery and for market acceptance. Such investigations on heat generation allow filling the research gap among SIB researchers for developing robust battery electrode material for mobile and storage applications. Exploring immoderate heat generation during electrochemical cycling is of scientific interest as well as beneficial for commercial usage. An excessive heat generation during the charging/discharging can lead to an accumulation of temperature inside the battery, which not only affects the performance and aging behavior of the batteries but also leads to unfavorable exothermal reactions causing thermal runaway [12,13]. Heat generation in electrochemical cells is divided into two main categories, namely reversible heat, and irreversible heat. The irreversible heat emerges from the internal ohmic resistance and polarization (exothermal reaction) of the cell and the reversible heat arises from the chemical reaction/entropic changes (endo-/exothermal reaction) in the host materials [14]. A small irreversible heat contribution is generated due to side reactions (parasitic/corrosion reactions) and during the formation of the solid electrolyte interphase (SEI) [15]. Heubner et al. [16], also have studies heat generation in porous LiCoO2 electrodes and found that total heat generation is significantly lower for charging compared to discharging due to the reversible heat and larger kinetic limitations for lithiated compared to de-lithiated LiCoO2. The electrochemical heat generation rate is usually a strong function of the current and state of the charge, with increases in the heat rate near the end of discharge/charge for low and high SOCs [17]. These temperature changes in the cell are because of electrochemical reactions, phase changes, mixing effects, and joule heating [18]. The magnitude of these heat values is closely related to the intrinsic properties of each component used in a SIB. Therefore, the fundamental understanding of heat generation in a SIB is of considerable importance for materials design to mitigate the intrinsic heat generation and improve the safety of the battery. In addition, to understand the contribution of different battery components to heat generation, various cycling studies accompanied by resistance investigations have a remarkable impact on the design of batteries. Electrochemical impedance spectroscopy (EIS) is a powerful tool for characterizing electrode processes in a short period of time. It has been utilized for analyzing the charge and mass transport properties of different fuel cells as well [19]. This method permits the distinction of diffusion in the host structure to electrolyte and charge transfer related resistances based on their time scales. Usually, the electrolyte conductivity can be observed at short time scales (high frequency), while charge transfer and solid-state diffusion are often observed at longer time scales (intermediate to low frequencies) [20]. The distribution of relaxation times (DRT) is a method to separate the polarization processes in the measured system in a better way than by a Nyquist or Bode plot [21]. DRT is used to identify the cathode and anode processes in an EIS measurement of a full cell, which was done for LIBs [22] and SIBs [23]. Within SIBs, the hard carbon anode material was investigated thoroughly with DRT to reveal the intercalation and plating processes [24]. A common strategy to distinguish the different processes is to use half cells [25,26] and/or symmetric cells [27]. DRTs for specific processes are the same in half and full cells and allow a classification of the respective electrode. The frequency-dependent impedance can be used to extract valuable information associated with cell operations by fitting an appropriate equivalent circuit model (ECM) [26].

The paper focuses on the development of sodium-ion cells which combine NASICON-based self-synthesized porous $Na_3V_2(PO_4)_3$/C positive electrode and coconut shell-derived commercial hard carbon (HC) as a negative electrode. Particular attention is given in this work to examining this system in terms of material degradation of cathode and anode materials. Subsequently, total heat generation during the cycling process is thoroughly investigated on fresh and cycle-aged cells. The different heat generation phenomena are identified and contributions of various resistances from cathode and anode are elucidated. For stationary energy storage systems with a long-running operation period, as well as for mobile applications and obvious for market acceptance, safety is a primary concern and must be considered. The current study intends to facilitate research on the way to develop safe sodium-ion batteries.

2. Experimental

2.1. $Na_3V_2(PO_4)_3$/C synthesis

The NVP/C composites were synthesized via spray-drying with a subsequent calcination process. For this, ammonium metavanadate (NH_4VO_3, Honeywell), sodium carbonate (VWR), and ammonium dihydrogen phosphate ($NH_4H_2PO_4$, VWR) were dispersed in absolute ethanol (VWR) in a molar ratio of 4:3:6. Polyacrylic acid (Sigma-Aldrich) and β-lactose (Sigma-Aldrich) were sub-joined with 16.7 wt %. The reactants were milled in a planetary ball mill for 5 h. The suspension was spray-dried with an inlet temperature of 150 °C and an outlet temperature of 95 °C. The resulting precursor powder was heated with a heating rate of 5 K/min to 400 °C and held for 4 h. Subsequently, the temperature was raised at the same rate to 850 °C followed by an isothermal dwell time of 12 h. A detailed characterization of the synthesized NVP/C powder was recently published [28] and material characterization analyses were presented in the supplementary materials (see Supplementary Fig. S1) in addition e.g., XRD, SEM, particle size distribution, and pore diameter of the NVP/C powder. The resulting porous NVP/C-compound includes 93 wt.-% $Na_3V_2(PO_4)_3$ and 7 wt.-% C and has an average particle size (d_{50}) of 16.6 μm.

2.2. Electrode coating

The cathode slurry was a mixture of 94 wt % NVP/C-compound, 3 wt.-% polyvinylidene fluoride binder (PVDF Solef 5130), 3 wt % carbon black (C-NERGY Super C65) in N-Methyl-2-pyrrolidon (NMP) solvent using a dissolver mixer (Dispermat, VMA Getzmann). The slurry was coated with a knife coating device in a roll-to-roll coater (KTF-S, Mathis AG) on an aluminum current collector (20 μm) followed by drying (80 °C and 120 °C) and calendaring. The anode was prepared similarly with the mass ratio of commercial coconut shell-derived hard carbon (HC), (93 wt %), carbon black (1.4 wt %), carboxymethyl cellulose (CMC) binder (1.87 wt %), and styrene butadiene rubber (SBR) binder (3.73 wt %) in a water solvent. The HC shows a specific surface area of 3.4 m^2/g, an average particle size (d_{50}) of 9 μm, and an interlayer spacing d_{002} of 0.401 nm.

2.3. Electrochemical measurements

The prepared $Na_3V_2(PO_4)_3$/C cathode sheets (mass loading of 1.1 mA/cm^2 (theoretical capacity of 117 $mAh.g^{-1}$)) and HC anode sheets (mass loading of 1.3 mA/cm^2 (theoretical capacity of 350 $mAh.g^{-1}$)), which leads to a cathode/anode capacity ratio of 1.18. The electrodes were implemented in small pouch cells (5 cm × 5 cm) in a dry room (dew point −65 °C) by adding 1 ml of 1 M $NaClO_4$ in EC:DMC:EMC (1:1:1 by volume) plus 2% FEC (by volume) electrolyte (Fosai new materials) and glass fiber separator (Whatman GF/A). The cells were cycled in a battery tester (Biologic EC-Lab, MPG 2) at 25 °C (Binder incubator) within the operating voltage window of 2.3–3.9 V. The pouch cells were formatted at 0.1C for 3 complete cycles with the 3rd stable cycle determining the actual specific cell capacity. The cycle stability tests were performed at a C-rate of 0.2C (charge/discharge) with a constant current profile with respect to the cathode mass loading. The capacity balancing and the activation procedure were adjusted with respect to the selected electrode materials, especially considering their

first cycle irreversible capacity. In the case of an imbalanced cell, the cathode/anode capacity ratio was 1:1.6 (excess of anode material, cathode mass loading remains steady).

Using the Biologic EC-Lab (MPG 2) cycler EIS measurements were made on CR2032 coin cells with electrodes diameter of 13 mm and 90 μl of electrolyte at states of charge (SOC) 0, 25, 50, 75, and 100% with the following test parameters: frequency range = 20 kHz–10 mHz, mode single sine, potential perturbation/sinus amplitude = 10 mV, points per decade = 6 at a temperature of 25 °C, the relaxation time of 1 h after each state of charge. DRT analyses were made based on the obtained impedance spectra with the RelaxIS 3 software. Furthermore, to understand the individual contributions of the anode and the cathode to the total impedance of the full cell, half cells with HC as well as $Na_3V_2(PO_4)_3$/C were assembled, and impedances were measured in the same way as for the full cells. The individual resistances of associated processes were obtained from fitting with an equivalent circuit model (ECM) consisting of a resistor connected in series to four Zarc elements as shown below in Fig. 1.

A single Zarc element consists of a resistor in parallel to a constant phase element (CPE). Thus, the free parameters are resistance R, time constant (relaxation time) τ, and CPE exponent. The first resistor comprises all pure ohmic resistances (measuring setup and electrolyte resistance), whereas the Zarc elements depict certain polarization processes. Resistance R times quasi capacitance Q of the CPE results in the time constant τ (or relaxation time of the process) [26]:

$$\tau_n = R_n Q_n = \frac{1}{2\pi f_n}$$

With frequency f_n at Zarc element n. The benefit of using Zarc is to extract the relaxation time from the DRT [29]. A Zarc element based on "Tau" represents the time constant of a circuit as a function of time when the system goes from one steady-state to another steady state. It has the advantage to anticipate in terms of time constant distributions (τ) rather than capacitance distributions. As a result, the true capacitance of a process can be calculated as $C = \tau/R$.

2.4. Heat generation analysis

Because the pouch cells did not fit into the MS80 3D Tian-Calvet calorimeter (MS80, Setaram Instrumentation, France), fresh coin cells from $Na_3V_2(PO_4)_3$/C vs HC with 1.0 mAh capacity were assembled from the same electrode sheets as used in pouch cell assembly. The coin cells were mounted in the coin cell holders and isolated with ceramic tape to prevent a short circuit. The coin cell holders were connected to the cycler (BioLogic BCS) with wires outside MS80 calorimeter (for instrumental setup, see Supplementary Fig. S2). There are four channels in the MS80 calorimeter (two sample channels, two reference channels), each measuring 32 mm in diameter, making it possible to conduct two coin cells test simultaneously. For weight equalization, a dummy coin cell with the same geometry was inserted into each reference channel. A differential signal between the samples and the references was recorded. The MS80 calorimeter has an advantage with the latest evolution of the calvet calorimetric 3D detector design to detect all forms of emit/absorb heat, including radiation, convection, and conduction. These calvet sensors can measure heat flow rate with high efficiency. The coin cells were used to determine the total generated heat under isothermal conditions at 25 °C. In the MS80 Tian-Calvet calorimeter their heat generation during cycling can be determined with great accuracy by direct heat flow measurement. The heat flow is determined by the 3D Tian-Calvet Sensor arrangement, where both the sample and the reference vessel are surrounded by rings with hundreds of thermocouples forming thermopiles. This leads to a sensitivity that allows recording heat flow values as little as 0.01 mW, which are typical for such small capacities of around 1 mAh. The related cycling data during the calorimetric experiment were recorded via a BioLogic instrument (BCS). The constant current, constant voltage (CCCV) with current (I) < C/20 or time >45 min test profile were applied both in charging (3.9 V) and discharging (2.3 V) with a rate of 0.2C. A 10 h relaxation period was introduced between each charge and discharge cycle in order to ensure that thermal equilibrium is reached. The same procedure was replicated for cycle-aged coin cells i.e., cycle-aged electrode sheets from pouch cells were utilized to assemble CR2032 coin cells followed by the above-mentioned heat generation test.

2.5. Post mortem analysis

The cycle-aged electrodes for EIS and heat generation analysis were punched out from the pouch electrodes (cycled) and rinsed with dimethyl carbonate (DMC) solvent. After drying at 70 °C for 24 h under vacuum (10^{-3} mbar), the full cells were assembled with the same amount of fresh electrolyte as employed in pristine coin cells. Before EIS measurements at the same SOCs as in the pristine state, the cells were formatted with 3 cycles at a 0.1C rate to get the actual capacity to set the SOC. The measurement procedure was the same as for pristine samples.

Scanning electron microscopy SEM (Supra 55, Zeiss) and Energy-dispersive X-ray spectroscopy (EDX) were made at cycle-aged electrodes that had been rinsed with DMC before. Cross-sections were prepared from the cathode with ion-beam milling (EM TIC3X, Leica Microsystems) in a pristine and cycle-aged state. A screw micrometer was used to determine the thicknesses of the electrode layers.

3. Results and discussion

3.1. Cycling stability

After formation (for formation cycles, see Supplementary Fig. S3), the pouch cell capacity was found to be ~18 mAh and cycling tests were conducted. A decent capacity retention of ~88% after 300 cycles can be observed in NVP/HC pouch cells at a charge/discharge rate of 0.2C. In the first 5 cycles, the capacity fading is relatively pronounced whereas the coulombic efficiency increases by over 99% (Fig. 2a). Beyond this running-in phase, the cycle stability is improved due to the insulating stable SEI film on the anode/cathode sides, similar to that as reported in lithium-ion batteries [30], that prevents further electrolyte decomposition and consumption of active materials. The potential profile of the full cell is shown in Fig. 2b for different cycles. The charge curve shows at first a slope region, which comes from the slope region of the HC. After about 5 mAh a plateau region is arising which is the overlapping of the plateau region of HC and NVP/C. The slope region is stable over the 300 cycles, but the voltage is slightly earlier increasing after the plateau region due to capacity degradation, which comes from completing the reaction at the cathode. The capacity degradation is therefore attributed to sodium loss over cycling.

3.2. Electrochemical impedance spectroscopy

Comparative charging curves of pristine (after formation cycles) and cycle-aged cells (300 cycles) with the corresponding Nyquist plots are depicted in Fig. 3. Substantial differences in the size of the semicircles can be seen, with the cycle-aged cell showing a noticeably larger size for

Fig. 1. Equivalent Circuit Model (ECM) including one resistor and four Zarc elements.

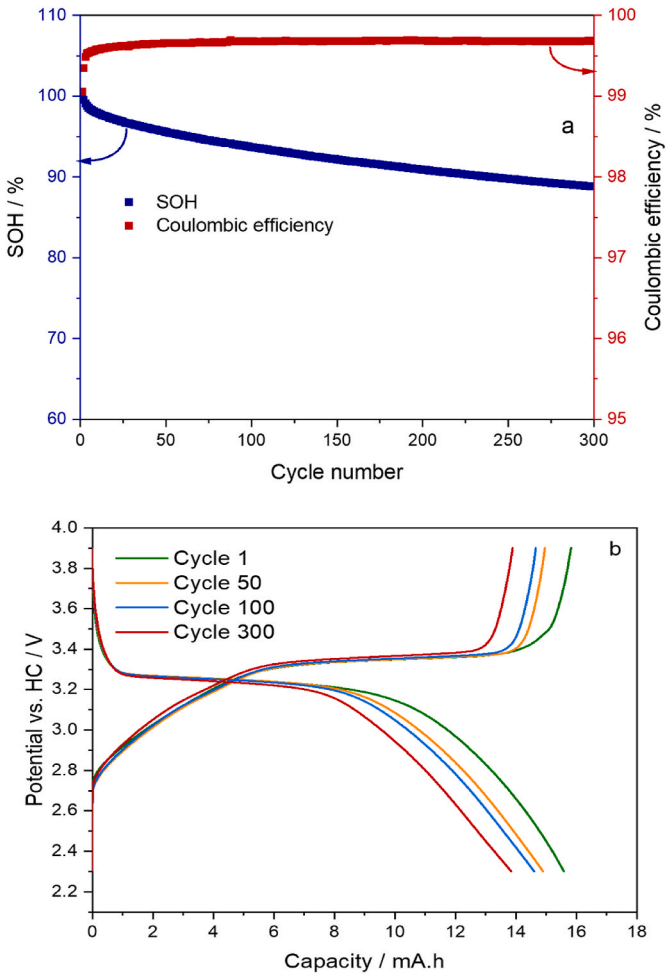

Fig. 2. Cycling performance of NVP/HC full pouch cell; (a) capacity fading and coulombic efficiency (b) charge/discharge profiles up to the state of health (SOH) 88% (0.2C rate, 300 cycles).

the mid-frequency semicircles at different SOCs. Two semicircles are observed in both impedance spectra, with the semicircle at high frequencies being significantly smaller.

In Fig. 4 the DRT and potential curves from NVP/Na, HC/Na, and (pristine and cycle-aged) NVP/HC cells are revealed. DRT of SOC at 0 and 100% are not shown due to an incomparability to SOC 25, 50 and 75% caused by deviating electrochemical processes in fully charged/discharged electrodes [31]. The DRT spectra, composed of five clearly distinguished peaks in the relaxation time range $\tau = 10^{-5} \ldots 10^{2}$ s, are attributed to distinct resistances such as the charge transfer resistance (R_{ct}), diffusion resistance (R_d), and passivation layer resistance (R_{SEI}) [19] enabling an assignment to specific materials and reactions. The peak marked "I" in the range $\tau = 10^{-5} \ldots 10^{-4}$ s seems to be a representation of the contact impedance between the electrode and the aluminum current collector. It is visible in all cells and cannot be attributed to a specific process. Peak "II" at around $\tau \sim 6{*}10^{-4}$ s is only existing in half cells, but not in full cells. Thus, this reaction occurs at the sodium metal anode. The peak "III" is detectable in all samples except for NVP/Na. Therefore, it can be attributed to the hard carbon. A different relaxation time for this peak in HC/Na in comparison to NVP/HC is the result of slightly deviating SOCs. For HC/Na, the capacity was calculated based on the mass of HC, whereas in the full cell the capacity was calculated with respect to the mass of NVP. Peak "IV" in the range $10^{0} \ldots 10^{1}$ s exists in all cells and contains contributions of NVP and HC. Peak "V" is located at high relaxation times of around $\tau = 10 \ldots 200$ s, a region, which is commonly related to solid diffusion within the active materials [26].

The positions of peak "I" and "II" do not show dependency on the SOC. However, peak "III" is shifted to lower relaxation times by increasing the SOC. At SOC 25%, HC is in the slope region of the potential curve, whereas at SOC 50% and SOC 75% it is in the plateau region (Fig. 4 f). This corresponds to different sodium intercalation mechanisms into the hard carbon (adsorbing into the micro pores and intercalation between graphene layers [32]). In the plateau region, the intercalation mechanism is the same, and therefore DRT at SOC 50% and SOC 75% are nearly identical. This is in accordance with the results of Schutjajew et al. [24] who found no significant changes in the DRT in the plateau region and concluded a kinetically homogeneous process related to the Na reduction. To clarify the contribution of peak "IV", resistance values are calculated from the curve-fit of NVP-Na and HC-Na cells (Fig. 4 g). The resistance at this relaxation time is below 10 Ω for HC-Na and 10 … 50 Ω for NVP-Na cell. It increases for both cells with increasing SOC. While at SOC 25% comparable contributions from both materials can be assumed yet, the higher SOC of 50% and 75% is dominated by NVP. With this knowledge, the assignment of the different DRT peaks can be summarized as:

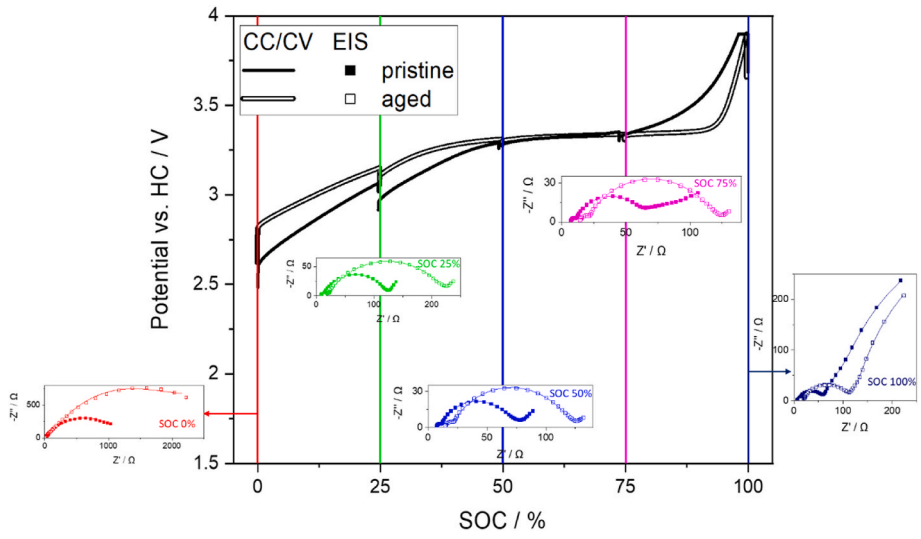

Fig. 3. Charging curves of pristine and cycle-aged NVP/HC cells with corresponding impedance spectra at selected SOC.

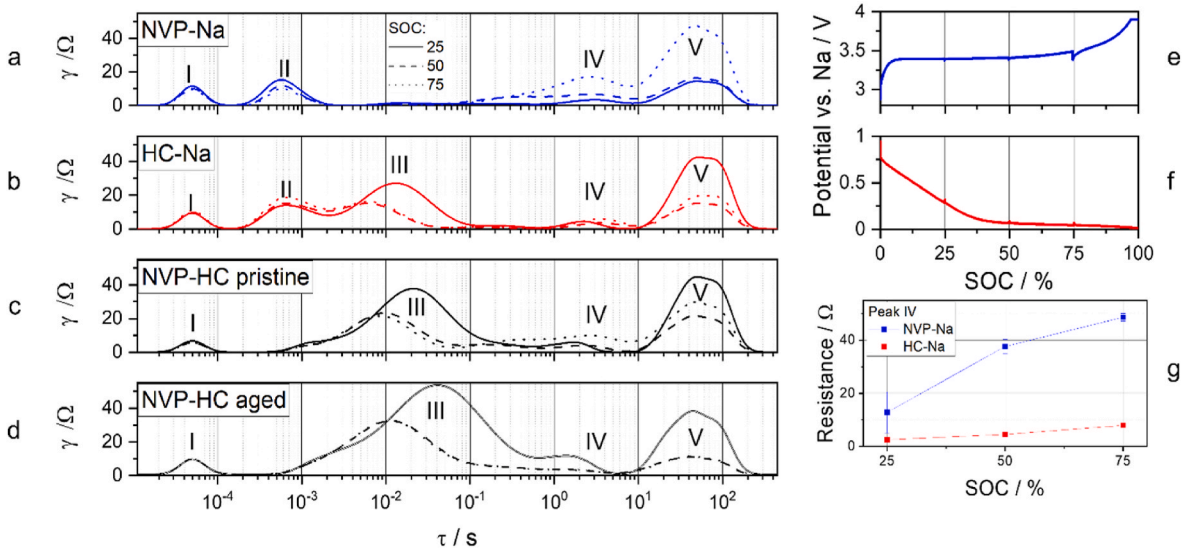

Fig. 4. DRT calculated from EIS measurements; a) NVP/Na, b) HC/Na, c) pristine NVP/HC, and d) cycle-aged NVP/HC cells at SOCs 25, 50 and 75%. Potential curves over SOC for e) NVP/Na, f) HC/Na cells, and g) resistance at peak "IV" for NVP-Na and HC-Na cells.

I → contact impedance between electrode film and current collector
II → charge transfer and/or SEI impedance of sodium metal electrode
III → charge transfer and/or SEI impedance of hard carbon electrode
IV → charge transfer impedance of NVP (with a minor contribution of HC)
V → diffusion of sodium in the solid phase (NVP and HC)

In Fig. 5 the results from the ECM fit are summarized for peaks "III" and "IV". In the pristine NVP/HC cell the peak "III", corresponding to the HC anode, decreases from 110 Ω at SOC 25% to around 50 Ω at SOC 50% and remains constant for SOC 75%, i.e., the charge transfer/SEI resistance of HC in the plateau region is lower than in the slope region. This trend is similar for the cycle-aged cell, but the peak "III" resistance is double as high as for the pristine cell. Peak "IV" rises in the pristine NVP/HC cell from nearly 0 Ω to 40 Ω as the SOC increases from 25% to 75%. This should be a result of the sodium depletion in the NVP.

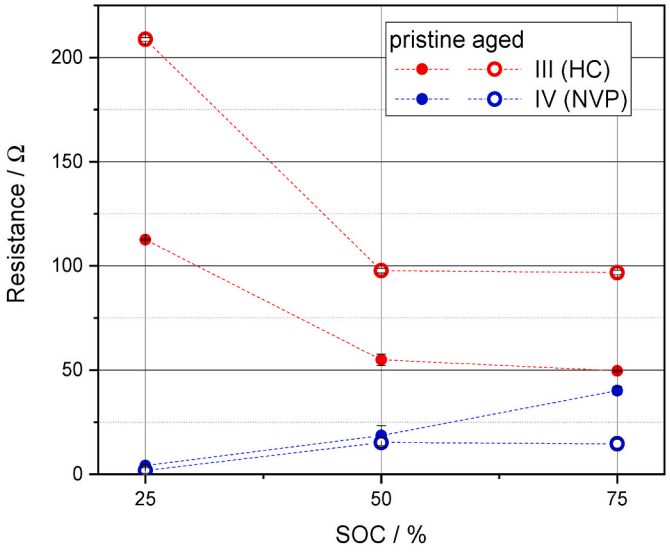

Fig. 5. Resistance of peak III and IV (see Fig. 4) obtained from EIS fitting with ECM (see Fig. 1) comparison between pristine and cycle-aged NVP/HC cells at SOC 25, 50, and 75%.

However, in the cycle-aged cell, the peak "IV" resistance initially increases too during charging to 50% but remains constant for SOC 75%. In SEM micrographs of the cycle-aged HC electrode (section 3.4, Fig. 8), sodium plating is visible. It leads to a growth of the SEI, which increases the resistance and leads to capacity loss. SEM cross-sections of NVP particles reveal no change between pristine and cycle-aged electrodes (Fig. 7) in particular, a formation of new cracks in the electrode layer or within the particles of the active cathode material cannot be detected. Due to this, most of the aging can be attributed to the anode.

3.3. Heat generation

For the heat generation test, the coin cells with the capacity of 1.0 mAh were assembled to get a sufficient heat flow signal with distinct slow charging/discharging rates of 0.2C in an MS80 calorimeter.

The charge/discharge cycles of pristine balanced and imbalanced as well as balanced cycle-aged NVP/HC coin cells are presented in Fig. 6a. In Fig. 6a, the green curve shows the charge/discharge profile of a balanced NVP/C-HC coin cell which shows a capacity of around 0.95 mA h. As all the coin cells are charged/discharged with the same current i.e., 0.2C rate, therefore the current curves are not shown in Fig. 6a. The red curve represents the charge/discharge of the imbalanced cell, and the orange curve depicts the cycle-aged charge/discharge capacities. The cycle-aged coin cell capacity is depleted to ~12% after 300 cycles as can be seen reduction in capacity to 0.83 mA h (Fig. 6a). Fig. 6b provides an insight into the operando heat flow measurement during the cycling of these cells with a 0.2C rate at 25 °C corresponding to their current-voltage profiles. The second loop was zoomed in for further detailed analysis along with the current-voltage profile (see Fig. 6c). In all full cells (Fig. 6b), the heat release rate of the cells becomes higher, when cells get close to SOC 100% and SOC 0%. These pronounced peaks can be assigned to the higher internal resistance of the cell. When the SOC becomes lower towards 0%, the internal resistance increases significantly resulting in an elevation of the irreversible heat inside the battery. Additionally, a significant decrease in the heat generation can be observed in the middle of the charging process of the full cells, which is mainly due to the plateau region (Fig. 6c). Lower heat generation during charge compared to discharge means that the reversible heat generation is endothermic during charge and exothermic during discharge. Hou et al. [33] studied the structural stability of HC and Zhang et al. [34] of NVP. They revealed the structural stability of electrode materials, which correlate to entropy change that contributes to reversible heat

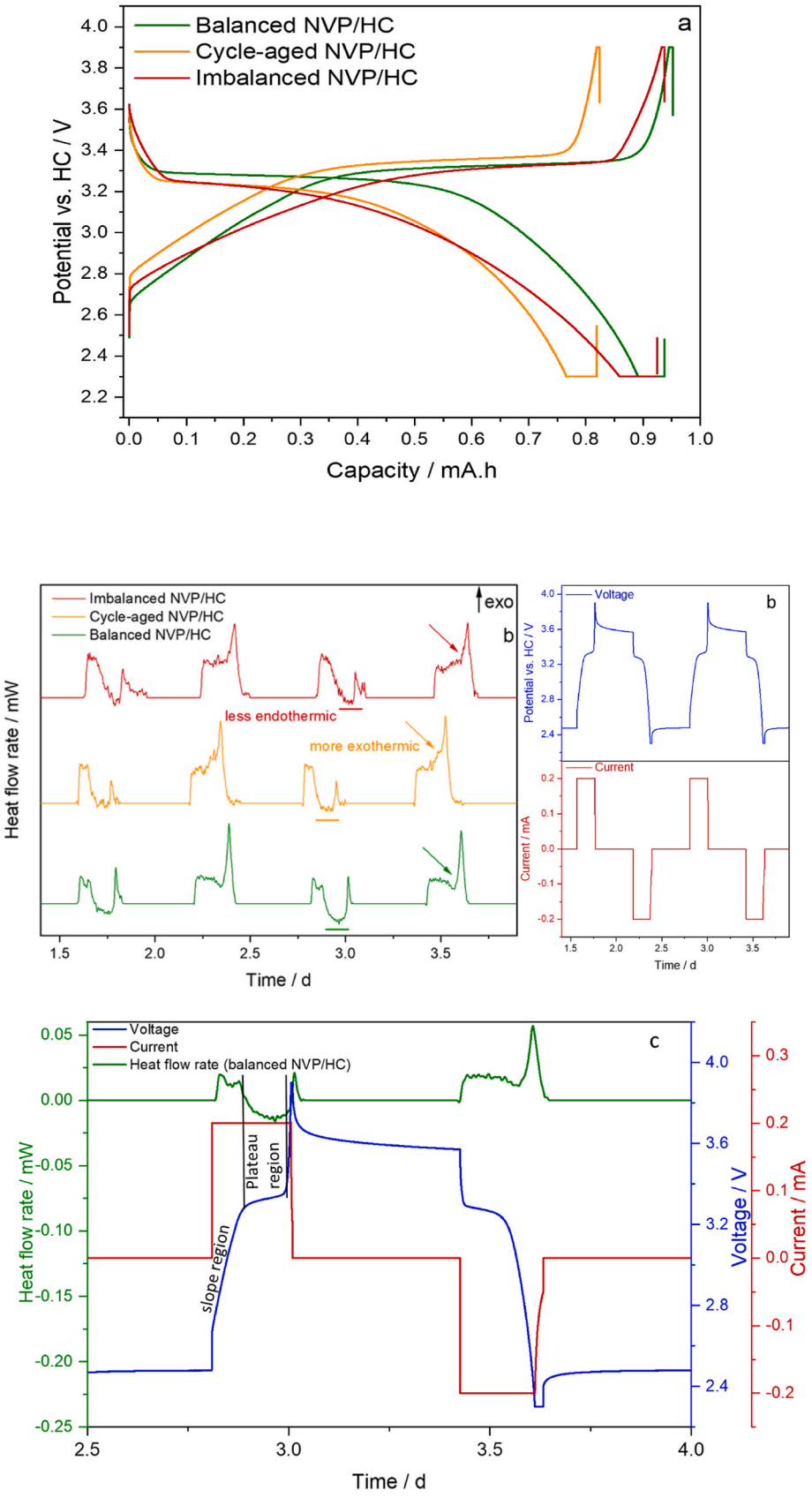

Fig. 6. Operando heat generation results for pristine/cycle-aged and imbalanced $Na_3V_2(PO_4)_3$/C vs HC in full coin cells using an MS80 Tian-Calvet calorimeter; (a) charge/discharge curves for NVP/HC full cells, (b) heat flow signals during charge/discharge (left) corresponding to their current-voltage profiles (right), (c) one loop of heat flow signals (pristine NVP/HC) with corresponding charge/discharge voltage and current.

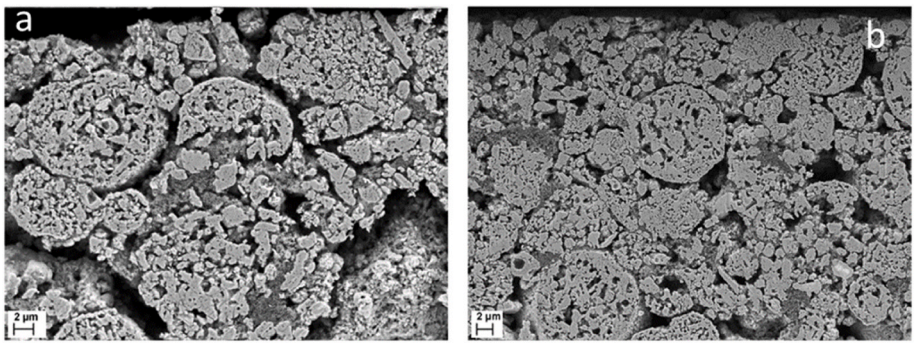

Fig. 7. SEM images of ion-milled cross-sections of a) Pristine $Na_3V_2(PO_4)_3$/C cathode sheet b) cycle-aged $Na_3V_2(PO_4)_3$/C cathode sheet.

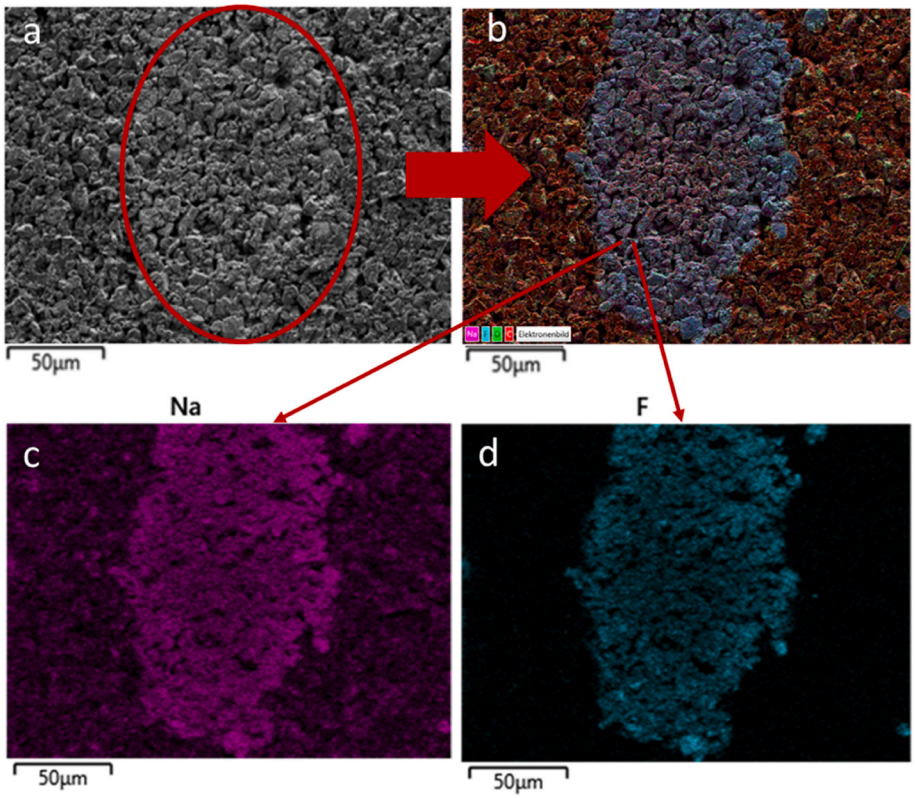

Fig. 8. SEM images of cycle-aged hard carbon anode surface; a) secondary electron image, b) EDX cartography of elemental mapping c) Na map and d) F map.

generation. Therefore, in our case the measured total generated heat during discharge is larger than during charge. At SOC 0% the overall impedances, in the beginning, are higher producing strong heat flow signals. In the charging phase, the heat was generated in particular in the slope region by the HC with the R_{SEI}/charge transfer resistances being relatively high. At SOC 50% which is in the plateau region, the heat flow signal tends towards endothermic and keeps the same trend till SOC 75% as no notable difference in R_{SEI}/R_{ct} resistances is found. From here to the end of the full charge (SOC 100%), a small exothermic peak appears again due to the solid-state diffusion resistance (R_e) (see Fig. 4), and it is obvious that the ohmic and polarization impedance rise at the end of charge as well. This can be clearly seen in the imbalanced cell where the

Table 1
Comparison of generated heat data during charging/discharging of fresh, imbalanced, and cycle-aged coin cells with 0.2C rate at 25 °C.

CR2032 Cell (1 mAh)	Charge capacity (mAh)	Discharge capacity (mAh)	Generated heat during Charge (J)	Generated heat during discharge (J)	Generated heat during charge (J)/Charge capacity (mAh)	Generated heat during discharge (J)/Discharge capacity (mAh)
0.2^{C} Pristine cell	0.95 ± 0.02	0.94 ± 0.01	0.15 ± 0.01	0.40 ± 0.01	0.16 ± 0.03	0.42 ± 0.02
0.2C Imbalanced cell	0.94 ± 0.03	0.93 ± 0.02	0.31 ± 0.05	0.51 ± 0.03	0.32 ± 0.08	0.54 ± 0.05
0.2C Cycle-aged cell	0.83 ± 0.003	0.82 ± 0.003	0.17 ± 0.002	0.55 ± 0.001	0.20 ± 0.005	0.67 ± 0.004

slope region is wider and the higher R_{SEI}/R_{ct} resistances (HC) cover a larger SOC range, and the plateau region is comparatively small contributing to a less expressed endothermic reaction (Fig. 6b). This results in a higher total generated heat in charge as well as in discharge phases, although the imbalanced cell capacity is more or less the same as in the balanced cell (see Table 1). These findings underline the high importance of cell balancing for cell design. The cycle-aged cell (Fig. 2), which was cycled to SOH ~88% reveals a significant increase in total generated heat in the discharge phase, as indicated in Fig. 6b and Table 1, due to the more expressed exothermal reaction. In the charging state, the cycle-aged cell shows an insignificant increase in the total generated heat due to a shorter slope pathway, which contributes more to an exothermic reaction. Since the cell is cycle-aged and ~12% capacity is already depleted, less time is needed to charge with a 0.2C rate (as 1C = 1 mAh). i.e., 4 h instead of 5 h (Fig. 6a). This can be seen in the last two columns of Table 1 where the generated heat per capacity is normalized. These data unveil a clear increase in the generated heat per capacity both in charge and discharge phases. Nevertheless. The heat generation is strongly morphology and electrode mass loading dependent, therefore in thicker electrodes, diffusion paths and resistances increase yielding more heat generation during cycling depending on charging/discharging rates.

The iR drop at various charge stages is tested and internal resistances are calculated (accordingly to the Galvanostatic cycling with potential limits (GCPL) curve in Fig. 3). The internal resistance at the SOC 0%, at the start, was higher and trends to decrease in the slopy region until SOC 25% and is calculated as 45Ω, which contributes to the heat generation as can be seen in Fig. 6c. Afterward, the internal resistance tends to decrease to 40 Ω at SOC 50% and stay the same at SOC 75% i.e., 40Ω. Therefore, the heat generation rate from SOC 50% to SOC 75% remains the same which is the plateau region where internal resistance is in a steady state. However, the sharp increase in heat flow rate is observed at SOC 100% which attributes to an increase in the internal resistance to 300Ω of the cell as an increase in the heat flow rate near the end of discharge/charge [17]. In the case of the cycle-aged cell, internal resistance at SOC 25% was 105Ω in the slopy region and the same heat flow signal trend is observed as in the pristine cell. At SOC 50% and SOC 75%, the internal resistances are the same as the values of 80Ω, however, heat resistances decrease with the increase of sodiation and at SOC 100% internal resistance in cycle-aged cell reached 600Ω. The same sharp heat flow signal is observed as in the case of the pristine cell. The iR-drop changes with the sodium concentration in NVP/C and HC. With cycle-aging, a prominent increase in internal resistances at various state of the charges are found (see Fig. S4).

3.4. Post-mortem analysis

The SEM images are shown in Fig. 7, the particles in the cycle-aged NVP (Fig. 7b) cathode look similar to the pristine particles (Fig. 7a). This can be confirmed by the nominal change in thickness of the positive electrode sheet and has already been discussed in the DRT analysis (section 3.2). In the literature, NVP shows extremely high cycle stability with low degradation over 1200 cycles [28]. However, at the cycle-aged HC surface, it seems that a sodium plating layer exists at distinct positions and not comprehensively over the whole anode surface. EDX analysis (Fig. 8) proves the presence of sodium and fluorine at the surface of the cycle-aged hard carbon electrode (Fig. 8c and d respectively). Hence an irreversible loss of sodium due to the consumption within the SEI layer [35] and sodium plating on the anode surface are the main aging factors. The measurement indicates a reaction with the FEC of the electrolyte to form a side product containing fluorine and sodium.

Thickness measurement of the hard carbon electrode shows that the cycle-aged anode strongly increased in thickness from 47 ± 1 μm (pristine) to 56 ± 1 μm (cycle-aged). In contrast, the cathode does not show remarkable growth in thickness i.e., from 81 ± 2 μm (pristine) to 83 ± 2 μm (cycle-aged). One possible explanation could be the growth of the SEI layer around each particle, which is observed in the EIS/DRT analysis where the charge transfer resistance (R_{SEI}/R_{ct}) increases. Additionally, the plating of sodium on the HC electrode sheet probably causes an increase in the thickness [36]. This capacity degradation mechanism was thoroughly investigated in lithium-based batteries and has been intensively reported in Refs. [37–40]. Moreover, Ma et al. [41] have studied and reported the associated capacity losses in different carbonate electrolyte systems due to solid electrolyte interphase formation and sodium diffusion in a sodium-ion battery.

4. Conclusions and outlook

A nanostructured porous $Na_3V_2(PO_4)_3$/C cathode material was utilized in combination with a commercial coconut-shell derived hard carbon as the anode material in sodium-ion cells of pouch and coin cell formats. In this study, the influence of cycle aging with respect to heat generation in a battery's lifetime has been investigated. This study explains that the cycle aging is predominantly driven by the sodium plating on the hard carbon electrode which affects the resistance of the entire system and results in increased heat generation of the battery during charging and discharging phases, which was confirmed by impedance studies as well. The total generated heat showed a pronounced increase in the imbalanced cell (excess of anode material), and this is noticeable evidence to take into consideration in cell design. The increase of the resistances revealed that it might be caused by the growth of the SEI layer that acts as a hindering layer which exhibits a remarkable increase of R_{ct} resistance in case of a cycle-aged cell and is limiting the diffusion kinetics. This paper focuses not only on heat generation in pristine and cycle-aged/degraded cells, but also describes the relationship between generated heat and degradation of materials.

The heat generation during the battery operation is important for the battery thermal management system (BTMS) where battery packs or cells during operation are at different states of charge and generate heat accordingly i.e., in endothermal or/and exothermic phases. Therefore, heat generation studies on cells facilitate managing thermal effects in efficient way in battery packs.

In further investigation, quantitative heats such as reversible (entropy) and irreversible heats will be separated in different sodium batteries and a comparison will be made between different cathode materials. This study is ongoing to help in the selection of safer cathode material and the result shall be published soon.

CRediT authorship contribution statement

Ijaz Ul Mohsin: Methodology, Validation, Formal analysis, Investigation, Writing – original draft, Visualization. **Luca Schneider:** Methodology, Validation, Formal analysis, Investigation, Writing – original draft, Visualization. **Marcel Häringer:** Formal analysis, Investigation, Writing – original draft, Visualization. **Carlos Ziebert:** Conceptualization, Writing – review & editing, Visualization, Supervision, Project administration, Funding acquisition. **Magnus Rohde:** Writing – review & editing, Supervision, Project administration. **Werner Bauer:** Writing – review & editing, Supervision. **Helmut Ehrenberg:** Writing – review & editing, Supervision. **Hans Jürgen Seifert:** Conceptualization, Writing – review & editing, Supervision, Project administration, Funding acquisition.

Declaration of competing interest

The authors declare that they have no known competing financial interests or personal relationships that could have appeared to influence the work reported in this paper.

Data availability

Data will be made available on request.

Acknowledgment

The authors gratefully acknowledge the support of S. Leuthner from Battery Technical Centre, for pouch cell assembly, C. Gebert for the MS80 3D Tian-Calvet calorimetry measurements, and Marcus Müller for the SEM/EDX analysis. This work contributes to the research performed at CELEST (Center for Electrochemical Energy Storage Ulm-Karlsruhe) and was funded by the German Research Foundation (DFG) under Project ID 390874152 (POLiS Cluster of Excellence, EXC 2154).

Appendix A. Supplementary data

Supplementary data to this article can be found online at https://doi.org/10.1016/j.jpowsour.2022.231901.

References

[1] https://cicenergigune.com/en/blog/critical-materials-battery-industry.
[2] J.-Y. Hwang, S.-T. Myung, Y.-K. Sun, Sodium-ion batteries: present and future, Chem. Soc. Rev. 46 (2017) 3529–3614.
[3] K.Z. Jiang, S. Xu, S.H. Guo, X.Y. Zhang, X.P. Zhang, Y. Qiao, T.C. Fang, P. Wang, P. He, H.S. Zhou, A phase-transition-free cathode for sodium-ion batteries with ultralong cycle life, Nano Energy 52 (2018) 88–94.
[4] P. Mei, Y.V. Kaneti, M. Pramanik, T. Takei, O. Dagc, Y. Sugahara, Y. Yamauchi, Two-dimensional mesoporous vanadium phosphate nanosheets through liquid crystal templating method toward supercapacitor application, Nano Energy 52 (2018) 336–344.
[5] R.R. Salunkhe, Y.V. Kaneti, Y. Yamauchi, Metal–Organic framework-derived nanoporous metal oxides toward supercapacitor applications: progress and prospects, ACS Nano 11 (2017) 5293–5308.
[6] R.R. Salunkhe, C. Young, J. Tang, T. Takei, Y. Ide, N. Kobayashi, Y. Yamauchi, A high-performance supercapacitor cell based on ZIF-8-derived nanoporous carbon using an organic electrolyte, Chem. Commun. 52 (2016) 4764–4767.
[7] Q. Zheng, H. Yi, X. Li, H. Zhang, Progress and prospect for NASICON-type $Na_3V_2(PO_4)_3$ for electrochemical energy storage, J. Energy Chem. 27 (6) (2018) 1597–1617.
[8] T. Lan, Q. Ma, C.L. Tsai, F. Tietz, O. Guillon, Ionic conductivity of Na3V2P3O12 as a function of electrochemical potential and its impact on battery performance, Batter. Supercaps. 4 (3) (2021) 479–484.
[9] W. Zheng, X. Huang, Y. Ren, H. Wang, S. Zhou, Y. Chen, X. Ding, T. Zhou, Porous spherical $Na_3V_2(PO_4)_3$/C composites synthesized via a spray drying -assisted process with high-rate performance as cathode materials for sodium-ion batteries, Solid State Ionics 308 (2017) 161–166.
[10] Y. Jiang, Z. Yang, W. Li, L. Zeng, F. Pan, M. Wang, X. Wei, G. Hu, L. Gu, Y. Yu, Nanoconfined carbon-coated $Na_3V_2(PO_4)_3$ particles in mesoporous carbon enabling ultralong cycle life for sodium-ion batteries, Adv. Energy Mater. 5 (10) (2015), 1402104.
[11] Z. Jian, L. Zhao, H. Pan, Y.-S. Hu, H. Li, W. Chen, L. Chen, Carbon coated $Na_3V_2(PO_4)_3$ as novel electrode material for sodium ion batteries, Electrochem. Commun. 14 (1) (2012) 86–89.
[12] H. Yang, S. Amiruddin, H. Bang, Y.K. Sun, J. Prakash, A review of Li-ion cell chemistries and their potential use in hybrid electric vehicles, J. Ind. Eng. Chem. 12 (2006) 12–38.
[13] R. Spotnitz, J. Franklin, Abuse behavior of high-power, lithium-ion cells, J. Power Sources 113 (2003) 81–100.
[14] J. Zhang, J. Huang, Z. Li, B. Wu, Z. Nie, Y. Sun, Comparison and validation of methods for estimating heat generation rate of large-format lithium-ion batteries, J. Therm. Anal. Calorim. 117 (2014) 447–461.
[15] S. Wang, Entropy and heat generation of lithium cells/batteries, Chin. Phys. B 25 (1) (2016), 010509.
[16] C. Heubner, M. Schneider, A. Michaelis, Detailed study of heat generation in porous LiCoO2 electrodes, J. Power Sources 307 (2016) 199–207.
[17] T.M. Bandhauer, S. Garimella, T.F. Fuller, A critical review of thermal issues in lithium-ion batteries, J. Electrochem. Soc. 158 (3) (2011) R1.
[18] D. Bernardi, E. Pawlikowski, J. Newman, A general energy balance for battery systems, J. Electrochem. Soc. 132 (1) (1985) 5–12.
[19] Z. Tang, Q.A. Huang, Y. Wang, F. Zhang, W. Li, A. Li, L. Zhang, J. Zhang, Recent progress in the use of electrochemical impedance spectroscopy for the measurement, monitoring, diagnosis and optimization of proton exchange membrane fuel cell performance, J. Power Sources 468 (2020), 228361.
[20] J.P. Schmidt, T. Chrobak, M. Ender, J. Illig, D. Klotz, E. Ivers-Tiffée, Studies on LiFePO4 as cathode material using impedance spectroscopy, J. Power Sources 196 (2011) 5342–5348.
[21] J.P. Schmidt, P. Berg, M. Schönleber, A. Weber, E. Ivers-Tiffée, The distribution of relaxation times as basis for generalized time-domain models for Li-ion batteries, J. Power Sources 221 (2013) 70–77.
[22] B. Manikandan, V. Ramar, C. Yap, P. Balaya, Investigation of physico-chemical processes in lithium-ion batteries by deconvolution of electrochemical impedance spectra, J. Power Sources 361 (2017) 300–309.
[23] L.U. Subasinghe, G. Satyanarayana Reddy, A. Rudola, P. Balaya, Analysis of heat generation and impedance characteristics of prussian blue analogue cathode-based 18650-type sodium-ion cells, J. Electrochem. Soc. 167 (2020), 110504.
[24] K. Schutjajew, T. Tichter, J. Schneider, M. Antonietti, C. Roth, M. Oschatz, Insights into the sodiation mechanism of hard carbon-like materials from electrochemical impedance spectroscopy, Phys. Chem. Chem. Phys. 23 (2021) 11488–11500.
[25] J. Illig, J.P. Schmidt, M. Weiss, A. Weber, E. Ivers-Tiffée, Understanding the impedance spectrum of 18650 LiFePO4-cells, J. Power Sources 239 (2013) 670–679.
[26] J.P. Schmidt, et al., Studies on LiFePO4 as cathode material using impedance spectroscopy, J. Power Sources 196 (2011) 5342–5348.
[27] B. Manikandan, V. Ramar, C. Yap, P. Balaya, Investigation of physico-chemical processes in lithium-ion batteries by deconvolution of electrochemical impedance spectra, J. Power Sources 361 (2017) 300–309.
[28] T. Akçay, M. Häringer, K. Pfeifer, J. Anhalt, J.R. Binder, S. Dsoke, D. Kramer, R. Mönig, $Na_3V_2(PO_4)_3$-A highly promising anode and cathode material for sodium-ion batteries, ACS Appl. Energy Mater. 4 (11) (2021) 12688–12695.
[29] T.H. Wan, M. Saccoccio, C. Chen, F. Ciucci, Influence of the discretization methods on the distribution of relaxation times deconvolution: implementing radial basis functions with DRTtools, Electrochim. Acta 184 (2015) 483–499.
[30] J. Xu, Y. Hu, T. liu, X. Wu, Improvement of cycle stability for high-voltage lithium-ion batteries by in-situ growth of SEI film on cathode, Nano Energy 5 (2014) 67–73.
[31] J. Landesfeind, D. Pritzl, H.A. Gasteiger, An analysis protocol for three-electrode Li-ion battery impedance spectra: Part I. Analysis of a high-voltage positive electrode, J. Electrochem. Soc. 164 (2017) A1773–A1783.
[32] L.F. Zhao, Z. Hu, W.H. Lai, Y. Tao, J. Peng, Z.C. Miao, Hard carbon anodes: fundamental understanding and commercial perspectives for Na-ion batteries beyond Li-ion and K-ion counterparts, Adv. Energy Mater. 1–28 (2020), 2002704.
[33] H. Hou, X. Qiu, W. Wei, Y. Zhang, X. Ji, Carbon anode materials for advanced sodium-ion batteries, Adv. Energy Mater. 7 (2017) 1–30.
[34] X. Zhang, X. Rui, D. Chen, H. Tan, D. Yang, S. Huang, Y. Yu, $Na_3V_2(PO_4)_3$: an advanced cathode for sodium-ion batteries, Nanoscale. R. Soc. Chem. 11 (2019) 2556–2576.
[35] B. Stiaszny, J.C. Ziegler, E. Krauß, M. Zhang, J.P. Schmidt, E. Ivers-Tiffée, Electrochemical characterization and post-mortem analysis of aged LiMn2O4–NMC/graphite lithium ion batteries part II: calendar aging, J. Power Sources 258 (2014) 61–75.
[36] T. Zheng, A.S. Gozdz, G.A. Amatucci, Reactivity of the solid electrolyte interface on carbon electrodes at elevated temperatures, J. Electrochem. Soc. 146 (1999) 4014–4018.
[37] P. Arora, R.E. White, M. Doyle, Capacity fade mechanisms and side reactions in lithium-ion batteries, J. Electrochem. Soc. 145 (1998) 3647–3667.
[38] M. Wohlfahrt-Mehrens, C. Vogler, J. Garche, Aging mechanisms of lithium cathode materials, J. Power Sources 127 (2004) 58–64.
[39] T. Zheng, A.S. Gozdz, G.A. Amatucci, Reactivity of the solid electrolyte interface on carbon electrodes at elevated temperatures, J. Electrochem. Soc. 146 (1999) 4014–4018.
[40] P. Ramadass, A. Durairajan, B. Haran, R. White, B. Popov, Studies on capacity fade of spinel-based Li-ion batteries, J. Electrochem. Soc. 149 (2002) A54–A60.
[41] L. Ma, A. Buckel, L. Nyholm, R. Younesi, Capacity losses due to solid electrolyte interphase formation and sodium diffusion in sodium-ion batteries, Research Square, Preprint (2021), https://doi.org/10.21203/rs.3.rs-623903/v1.